Laminar-Turbulent Transitional Flow Phenomena in Isosceles Triangular Cross-Section Ducts

RICHARD W. HANKS and RICHARD C. COPE

Brigham Young University, Provo, Utah

A theoretical analysis of the laminar-turbulent transition phenomenon is presented for the case of steady, isothermal, fully developed flow of Newtonian fluids in straight ducts of constant isosceles triangular cross section. As a result of this analysis, the simultaneous existence of macroscopically large stable regions of laminar and turbulent flow are predicted to occur during the transition phenomenon. The existence of this special type of flow field, which has not been previously predicted theoretically, is shown to be a consequence of the presence of an asymmetric shear stress distribution. The results of an experimental study are also presented. These data verify the predictions made by the theoretical analysis.

Sparrow's theoretical study (*1*) of laminar flow and Eckert and Irvine's (*2*) experimental study of transitional flow in isosceles triangular ducts suggest the existence of some rather interesting phenomena in the transitional flow range for such ducts. The purpose of this paper is to present the results of a theoretical analysis and experimental investigation of the transition phenomenon in isosceles triangular ducts and to demonstrate the existence of a unique and heretofore theoretically unpredicted phenomenon in this flow region.

REVIEW OF PREVIOUS RESEARCH

Eckert and Irvine (*2*) presented data obtained from a flow visualization study of air flow in isosceles triangular ducts which they interpreted as showing the existence of a range of flows for which there occurred simultaneous macroscopically large regions of laminar and turbulent flow in the duct. This is not to be confused with the traditional concept of a laminar sublayer in turbulent flow. Rather, what is implied is a macroscopically large region of the flow field which experiences turbulent flow side by side with a separate macroscopically large region which is in stable laminar flow. Such a duality of mode is furthermore independent of time at a given spatial location.

The existence of such a dual flow region implies that the frictional resistance of the duct should be increased over that due to laminar flow because of the turbulence present, but decreased from the turbulent value because of the laminar flow present. However, such a region of frictional flow resistance behavior is not evident in the data of Carlson and Irvine (*3*) who studied the frictional resistance of air flow in a series of isosceles triangular ducts similar to the ones used by Eckert and Irvine (*2*). Hanks and Brooks (*4*), using a flow birefringence technique, showed that Eckert and Irvine's (*2*) interpretation of their flow visualization data was due primarily to the influence of their probe wake.

As a result of the above observations, it is unclear just what phenomena are to be expected in transitional flow in triangular ducts. Sparrow's theoretical (*1*) analysis of laminar flow in such ducts makes possible the theoretical analysis of the laminar turbulent transition problem. That analysis, involving application of Hanks' theory (*5, 6*) of laminar flow stability, follows.

THEORETICAL ANALYSIS

It has been shown (*5, 6*) that the stability* of a rectilinear flow field in a duct of fixed boundaries is determined by the condition that the parameter

$$K = \rho \frac{|\nabla (\frac{1}{2}v^2)|}{|\rho \mathbf{f} - \nabla p|} = 404 \qquad (1)$$

where the absolute value signs | | imply magnitudes of the vectors enclosed thereby. For a rectilinear flow in a duct of isosceles triangular cross section, such as illustrated schematically in Figure 1, Equation (1) can be reduced to

* In the presence of strong inlet disturbances, it was shown (*6*) that for such a field the necessary and sufficient condition for transition to turbulence is the existence of flow profile instability.

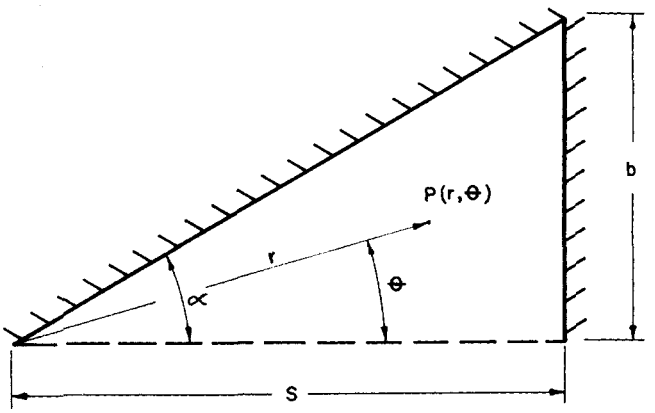

Fig. 1. Coordinate geometry of isosceles triangular cross-section duct. Lower half of duct is mirror image of portion shown about altitude s as a line of symmetry.

$$404 = \frac{\rho\, v_z \left[\left(\frac{\partial v_z}{\partial r} \right)^2 + \left(\frac{1}{r} \frac{\partial v_z}{\partial \theta} \right)^2 \right]^{1/2}}{-dp/dz} \qquad (2)$$

by using the polar coordinate system located at the apex as illustrated in Figure 1. This expression may be made dimensionless as follows:

$$404 = \frac{\rho <v_z> c^2}{s\,(-dp/dz)_c} F(\bar{\xi}, \bar{\theta}) \qquad (3)$$

where $F(\bar{\xi}, \bar{\theta})$ is $F(\xi, \theta)$ evaluated (5, 6) at the points $\xi = \bar{\xi}$ and $\theta = \bar{\theta}$ corresponding to the maxima of the function

$$F(\xi, \theta) = u \left\{ \left(\frac{\partial u}{\partial \xi} \right)^2 + \left(\frac{1}{\xi} \frac{\partial u}{\partial \theta} \right)^2 \right\}^{1/2} \qquad (4)$$

where $u \equiv v_z/<v_z>$ and $\xi \equiv r/s$. In Equations (3) and (4), $<v_z>$ is the area mean velocity $\frac{1}{A}\int_A v_z dA$. In order to evaluate $F(\bar{\xi}, \bar{\theta})$, one thus requires an expression for $u(\xi, \theta)$.

Sparrow (1) presents expressions for $u(\xi, \theta)$ as follows:

$$u(\xi, \theta) = \frac{1}{G(\alpha)} \left\{ \xi^2 \left(\frac{\cos 2\theta}{\cos 2\alpha} - 1 \right) + \sum_{j=1}^{N} c_j \xi^{\lambda_j} \cos \lambda_j \theta \right\}$$

$$\lambda_j = \frac{2j-1}{2} \frac{\pi}{\alpha} \qquad (5)$$

$$G(\alpha) = \frac{1}{3} \left(\frac{1 - \cos 2\alpha}{\cos 2\alpha} \right) + \frac{2}{\tan \alpha} \sum_{j=1}^{N} \left\{ c_j (2 + \lambda_j)^{-1} \cdot \int_0^{\alpha} \frac{\cos \lambda_j \theta}{(\cos \theta)^{2+\lambda_j}} d\theta \right\} \qquad (6)$$

where N is a finite upper limit (1) to the series and c_j and λ_j are, respectively, Fourier coefficients and eigenvalues derived by an approximation technique. In terms of these results, one can write Equation (3) as

$$(N_{Re})_c = \frac{3232 \sin \alpha}{(1 + \sin\alpha)\, G(\alpha)} \frac{1}{F(\bar{\xi}, \bar{\theta})} \qquad (7)$$

where $(N_{Re})_c = D_H <v_z>_c \rho/\mu$ is the critical Reynolds number, and $D_H = 2s \sin \alpha/(1 + \sin \alpha)$ is the conventional hydraulic diameter.

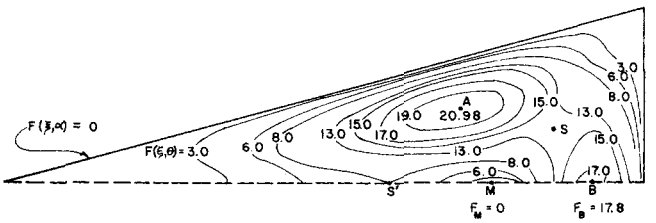

Fig. 2. Theoretically computed contours of constant $F(\xi, \theta)$ for isosceles triangular duct having apex half angle $\alpha = 15$ deg. $F(\xi, \theta)$ is defined by Equations (4) to (6). Points A and B are relative maxima, points S and S' are saddle points, and point M is a minimum point.

One must thus determine the value(s) of $F(\bar{\xi}, \bar{\theta})$ from Equations (4) to (6). The analytical equations for this purpose (7) are rather cumbersome algebraically and numerically, and consequently, a simpler method (8) was used to determine $\bar{\xi}$, $\bar{\theta}$ and $F(\bar{\xi}, \bar{\theta})$. The function $F(\xi, \theta)$ was computed for a grid of values ξ, θ. From a rough grid map of the entire cross section,* the points of maximum $F(\xi, \theta)$ are readily localized. For these subregions, the calculation is repeated for successively smaller mesh increments in ξ, θ until $F(\bar{\xi}, \bar{\theta})$ and $\bar{\xi}$, $\bar{\theta}$ are obtained to the desired degree of numerical precision. These values are then used in Equation (7) to calculate $(N_{Re})_c$.

Figure 2 is a sample of the function $F(\xi, \theta)$ for the case $\alpha = 15$ deg. From this contour plot, several interesting observations may be made. Because of the nature of the parameter K, it follows that $F(\xi, \theta) = 0$ along the boundaries because $v_z = 0$. Also $F(\xi, \theta) = 0$ at point M because $\partial v_z/\partial r = \partial v_z/\partial \theta = 0$. Because of this feature and the positive definiteness of K, three relative maxima and three saddle points are observed. Points A (the lower half of the flow field is a mirror image of Figure 2) and B are the maxima, and points S and S' are the saddle points.

From Figure 2 it is clear that $F_A(\bar{\xi}, \bar{\theta}) > F_B(\bar{\xi}, \bar{\theta})$. That is, points A are less stable than point B. This result is general for $\alpha < 30$ deg. and arises quite naturally from Sparrow's (1) velocity profile equations which show the wall shear stress to be higher near the oblique walls of the duct for the case in question than for the base wall. The reverse situation obtains for $\alpha > 30$ deg.

The above result leads one immediately to the conclusion that turbulence may be initiated first near points A in small angle ducts. Therefore, since $F_A/F_B > 1$, there may exist a significant, and, therefore, probably measurable, range of Reynolds numbers for which turbulent flow will exist in the region above a curve through points M, S and the base vertexes of the triangle, while laminar flow simultaneously exists in the region below this curve (near point B). Furthermore, this laminar region should be stable, causing disturbances to be damped out, while disturbances introduced near points A should grow and persist as turbulence.

This region of simultaneous side by side laminar and turbulent flow should give rise to an increase in frictional resistance which will be intermediate to that expected for full turbulence. This increase in frictional resistance should, therefore, cause a plot of f times N_{Re} as a function of N_{Re} to assume the qualitative shape illustrated schematically in Figure 3. The horizontal line for $N_{Re} < (N_{Re})_{c1}$ corresponds to the unique product of fN_{Re} for laminar flow.†

* Actually, only half of the cross section is used because of symmetry.
† This constant is obtained from the solution of the equations of motion.

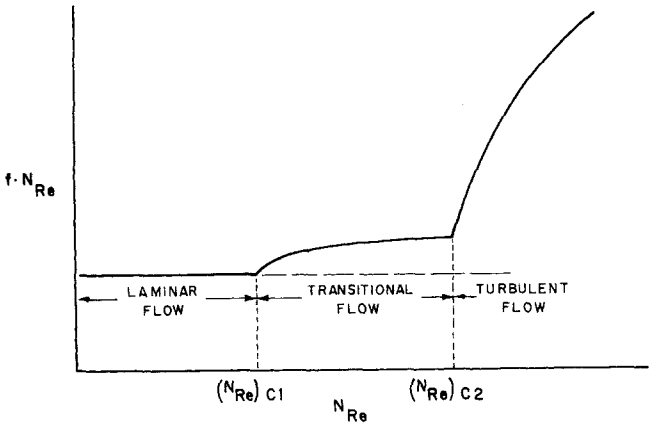

Fig. 3. Schematic representation of frictional resistance curve for isosceles triangular duct as predicted theoretically. This curve illustrates the significance of the lower and upper critical Reynolds numbers.

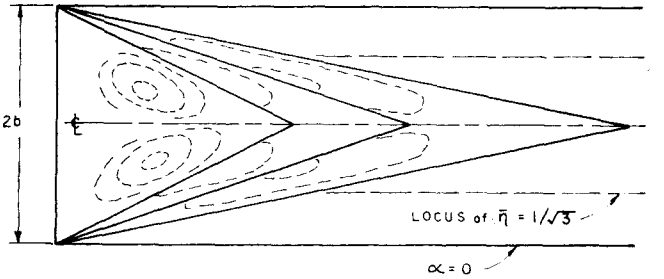

Fig. 4. Schematic representation of behavior of critical location $\bar{\theta}$ for which $F(\bar{\xi}, \bar{\theta})$ obtains its greatest relative maximum value as the apex half angle α tends toward zero. Location is expressed in dimensionless form as $\bar{\eta} = \bar{\theta}/\alpha$. Limiting value $\sqrt{1/3}$ is characteristic of flat plate geometry.

When K reaches its critical value corresponding to the highest relative maximum value of $F(\xi, \theta)$, the unstable part of the flow will undergo transition to turbulence, causing a rise in the $f \cdot N_{Re}$ product. This condition is indicated by the dashed line at $(N_{Re})_{c1}$ in Figure 3. This value of the Reynolds number is called the *first* or *lower* critical Reynolds number. As the flow rate increases, eventually a value will be reached for which the magnitude of K at the lower relative maximum* of $F(\xi, \theta)$ will correspond to instability, and the remainder of the flow will become turbulent with a resultant large increase in fN_{Re}. This latter transition, called the *second* or *upper* critical Reynolds number, is indicated in Figure 3 by the dashed line at $(N_{Re})_{c2}$.

Two interesting special cases arise as a result of the above considerations. These are the equilateral ($\alpha = 30$ deg.) case for which the shear stress distributions are identical on all three boundaries, and the limiting behavior for very small apex angles ($\alpha \to 0$).

In the equilateral duct case, the three relative maxima in $F(\xi, \theta)$ have identical magnitudes, suggesting that perhaps only a single transition Reynolds number should be observed, since all three regions of the flow become simultaneously unstable. This would suggest that $(N_{Re})_{c1} = (N_{Re})_{c2}$ for the equilateral duct. However, this last hypothesis must be considered as only tentative, since the lack of a theory for the turbulent flow field precludes a complete analysis of the influence of the nonuniform wall shear stress field. Since the stress field in the equilateral triangular duct is still highly nonuniform (*1*), albeit symmetric, it differs significantly from the stress fields of either a round pipe or flat parallel plates, both of which are symmetric and uniform, and for both of which only a single critical Reynolds number is observed. The answering of this question must be based upon consideration of experimental data.

A much more definite prediction may be made concerning the behavior of isosceles triangular ducts for very small apex angles as α approaches zero. Figure 4 is a schematic representation of the behavior of the location $\bar{\theta}$ for which $F(\bar{\xi}, \theta)$ attains its highest relative maximum magnitude as the base of the triangle is held constant while the apex is removed to infinity. The quantitative variation of $\bar{\theta}/\alpha$ with decreasing α is shown in Figure 5. The circled points were calculated from Sparrow's velocity profiles by the above procedure. It is clear from Figures 4 and 5 that in the limit of small apex angles the isosceles triangular duct approaches a type of behavior similar to flat parallel plates. The exact form of behavior becomes evident from a limiting analysis of Sparrow's solution of the equations of motion which may be rewritten as follows:

$$u = \frac{fN_{Re}(1+\sin\alpha)^2}{4\cos^2\alpha(1-\tan^2\alpha)}\left[\left(\frac{x}{b}\tan\alpha\right)^2 - (y/b)^2\right] + \frac{fN_{Re}(1+\sin\alpha)^2}{8\sin^2\alpha}\sum_{j=1}^{N} c_j\,\xi^{\lambda_j}\cos\lambda_j\theta \quad (8)$$

$$fN_{Re} = 12\left\{\frac{(1+\sin\alpha)^2}{\cos^2\alpha(1-\tan^2\alpha)} + \frac{4\alpha(1+\sin\alpha)^2}{\tan\alpha\sin^2\alpha}\sum_{j=1}^{N}\frac{c_j I_j}{(2j-1)\pi+4\alpha}\right\} \quad (9)$$

$$I_j = \int_0^{\alpha}\frac{\cos\lambda_j\theta}{(\cos\theta)^{2+\lambda_j}}\,d\theta; \quad \lambda_j = (2j-1)\frac{\pi}{2\alpha} \quad (10)$$

Now, as $\alpha \to 0$, these equations reduce* to

$$u = 3[1-(y/b)^2] \quad (11)$$

$$fN_{Re} = 12 \quad (12)$$

since $I_j\ (\alpha \to 0) \to 0$. Also, the hydraulic diameter $D_H = 2b\cos\alpha/(1+\sin\alpha) \to 2b$ as $\alpha \to 0$. From these results, then, it is clear that as $\alpha \to 0$, $(N_{Re})_{c1} \to (N_{Re})_{c2}$, and both must approach a common value $(N_{Re})_c$ based on $D_H = 2b$. This limiting value can be calculated from Equations (4) to (7) and (11) for limiting values of α. In computing the limiting value of $(N_{Re})_c$, it is useful to note that

$$\lim_{\alpha\to 0} G(\alpha) = \frac{2}{3}\,\frac{\tan^2\alpha}{1-\tan^2\alpha} \quad (13)$$

Thus, from Equation (7) it follows that

$$(N_{Re})_c \to \frac{4848\cos\alpha\,(1-\tan^2\alpha)}{(1+\sin\alpha)\tan\alpha\,F_0(\bar{\xi},\bar{\theta})} \quad (14)$$

* Actually, once transition has occurred in part of the duct, the existence of turbulence there will influence the velocity profile in the remaining stable portion, and the $F(\xi, \theta)$ calculations made above will not be quantitatively valid. Since no theory exists which will permit computation of the turbulent field in the part of the flow already having undergone transition, one is unable to make a quantitative calculation of the transitional fN_{Re} curve.

* In Equation (8), x and y are a set of Cartesian coordinates related to r and θ by $x = r\cos\theta$ and $y = r\sin\theta$. In evaluating the limit of Equation (8) as $\alpha \to 0$, one must recognize that $\theta \to 0$ also, and hence $x = r\cos\theta \to r\cos\alpha = b/\tan\alpha$, where b is the half separation of the plates or half base of the triangle. Thus, the quantity $x\tan\alpha/b \to 1$ as $\alpha \to 0$ and Equation (11) follow directly.

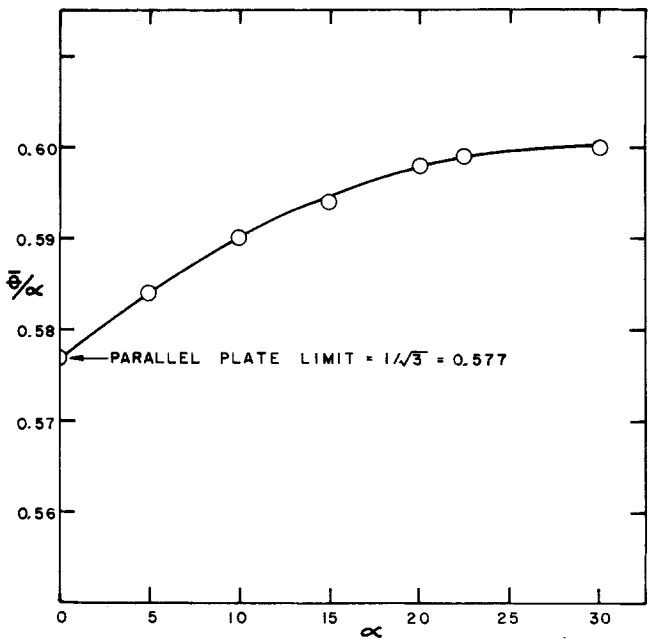

Fig. 5. Quantitative variation of $\overline{\theta}/\alpha$ as a function of apex half angle α as computed theoretically.

where $F_0(\overline{\xi}, \overline{\theta})$ is the limiting form of $F(\overline{\xi}, \overline{\theta})$ near $\alpha = 0$. By using the polar coordinate transformation to convert Equation (4) from $F(\overline{\xi}, \overline{\theta})$ to $F(x, y)$ and by noting that in the limit $\alpha \to 0$, $\cos\theta \to 1$, $\sin\theta \to 0$, and $|\partial u/\partial x| << |\partial u/\partial y|$, one finally observes that

$$\lim_{\alpha \to 0} \tan\alpha \; F(\overline{\xi}, \overline{\theta}) \to u(\overline{\zeta}) \left| \frac{du}{d\zeta} \right|_{\overline{\zeta}} \qquad (15)$$

where $\zeta = y/b$, and $u(\zeta)$ is given by Equation (11). Since $\theta \to 0$, one can replace θ/α by y/b as a good approximation, and hence $\overline{\zeta} = \overline{\theta}$ $(\alpha \to 0) = \sqrt{1/3}$ from the previous arguments. Thus, one finds that

$$\lim_{\alpha \to 0} \tan\alpha \; F(\overline{\xi}, \overline{\theta}) = 12\sqrt{1/3} \qquad (16)$$

and hence

$$\lim_{\alpha \to 0} (N_{Re})_c = 404\sqrt{3} = 700 \qquad (17)$$

Since the geometry of K is such that only a single maximum occurs in the domain when $\alpha \to 0$, it follows that there can be only one value for $(N_{Re})_c$, and hence $(N_{Re})_{c1} = (N_{Re})_{c2} = (N_{Re})_c$ as given by Equation (17). An interesting observation one may make concerning this limiting isosceles triangle is that if one compares it with a limiting rectangle of height $2b$ and infinite width, one finds that for the critical Reynolds number condition $(N_{Re})_c$ (triangle) = $\frac{1}{4}(N_{Re})_c$ (rectangle), f_c (triangle) = $2f_c$ (rectangle), $\langle v \rangle_c$ (triangle) = $\frac{1}{2}\langle v \rangle_c$ (rectangle) and $(-dp/dz)_c$ (triangle) = $(-dp/dz)_c$ (rectangle). Thus, although the critical pressure gradients are identical, none of the other flow variables are. That this should be so is rather easily seen if one realizes that the isosceles triangle of base $2b$ has a flow area one half that of a rectangle of height $2b$ and width s (the height of the triangle), and this relation holds true as $s \to \infty$ $(\alpha \to 0)$. As the surface area of the triangle approaches that of the rectangle per unit length, its included volume is only half that of the rectangle. Thus, even though geometrically the isosceles triangle appears to approach flat parallel plates as $\alpha \to 0$, the flow behavior is quite different.

Sparrow (*1*) only presents c_j values for apex angles down to $\alpha = 5$ deg. In order to compute the curve of $(N_{Re})_{c1}$ (α) for $0 < \alpha < 5$ deg., two alternatives are open. One could repeat Sparrow's computation scheme (*1*) to calculate c_j's for these angles followed by the present calculation for $F(\overline{\xi}, \overline{\theta})$. Alternatively, one can recognize that the solution of Eckert and Irvine (*2*) for the circular sector can be written subject to the condition that the sector

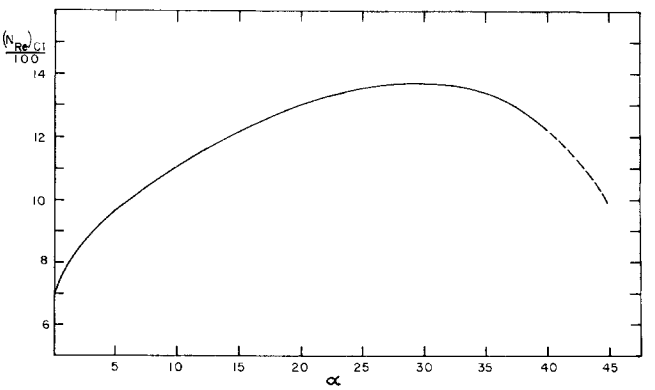

Fig. 6. Theoretically computed variation of $(N_{Re})_{c1}$ as a function of apex half angle α.

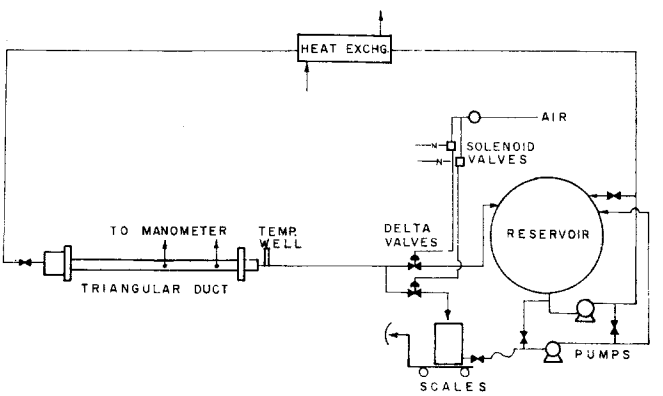

Fig. 7. Schematic flow diagram of experimental test loop.

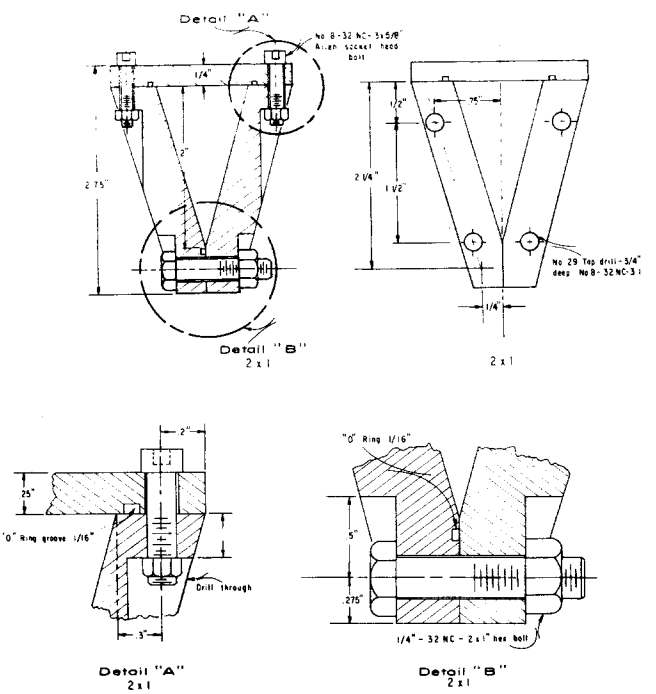

DETAILS of TRIANGULAR DUCT

Fig. 8. Design details of triangular test ducts.

area equal that of an isosceles triangle of equal apex angle. This is accomplished (*1*) by setting $R^2 = s^2 \tan\alpha/\alpha$, where R is the sector radius. Thus, Eckert and Irvine's result (*2*) becomes

$$\frac{2D_H^2}{fN_{Re}} \frac{v_z}{\langle v_z \rangle} = \xi^2 \left[\frac{\cos 2\theta}{\cos 2\alpha} - 1 \right] + \sum_{j=1}^{\infty} \beta_j \xi^{\frac{2j-1}{2}} \frac{\pi}{\alpha} \cos(2j-1)\frac{\pi}{2}\frac{\theta}{\alpha} \quad (18)$$

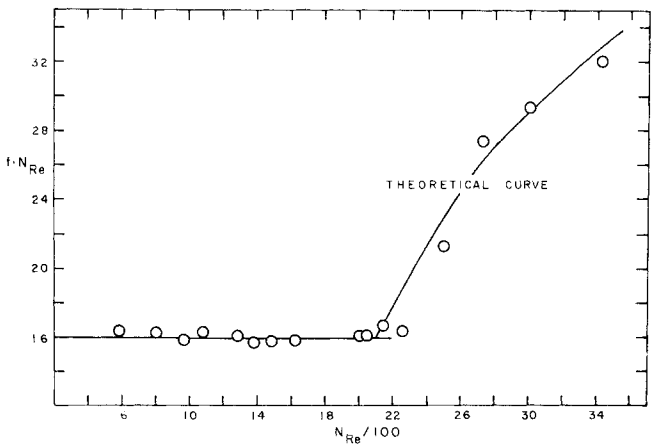

Fig. 9. Preliminary pipe flow data obtained to test precision and accuracy of measuring instruments. Data are compared with theoretical curves.

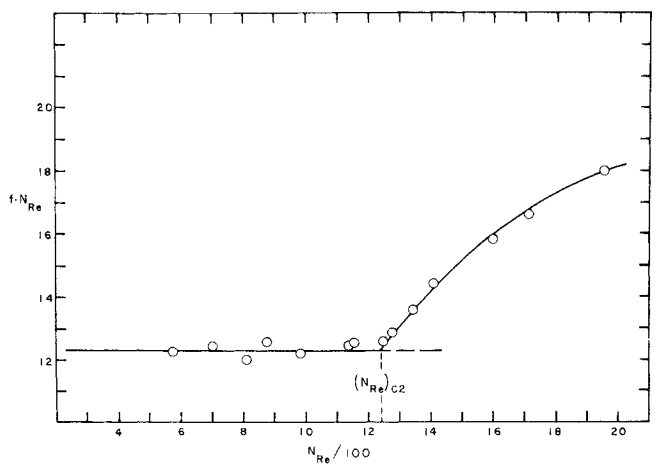

Fig. 10. Experimental friction loss data obtained in $\alpha = 2.5$ deg. duct.

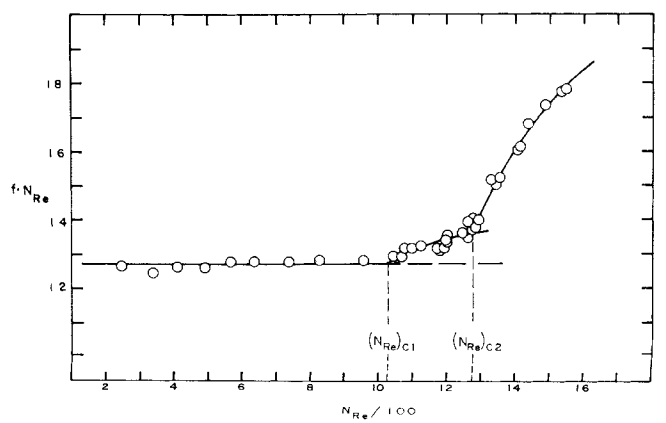

Fig. 11. Experimental friction loss data obtained in $\alpha = 7.5$ deg. duct.

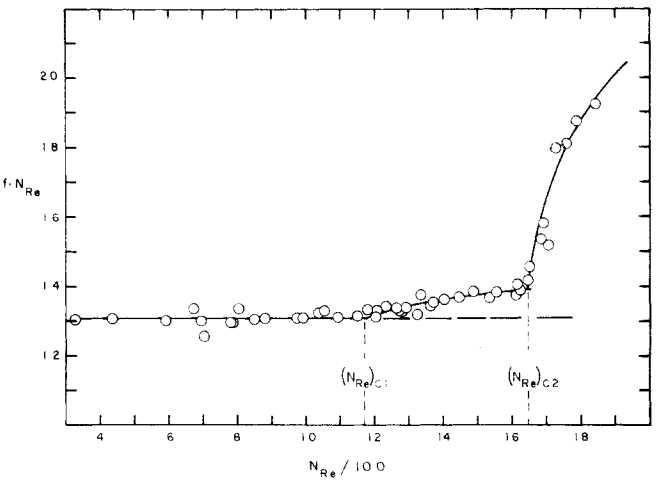

Fig. 12. Experimental friction loss data obtained in $\alpha = 15$ deg. duct.

$$\beta_j = \frac{64}{\pi^3} \alpha \tan\alpha \frac{(-1)^j [\alpha/\tan\alpha]^{(2j-1)\ \pi/4\alpha}}{(2j-1)\left[(2j-1)^2 - \frac{16\alpha^2}{\pi^2}\right]} \quad (19)$$

Since in Equation (5) $u(\xi, \theta)\, G(\alpha) = 2D_H^2 (v_z/\langle v_z \rangle)/fN_{Re}$, it follows that Equations (5) and (14) are identical if $\lim_{\alpha \to 0} c_j = \beta_j$. In fact, Sparrows' approximation scheme (*1*) for obtaining the c_j values is equivalent to fitting Equation (18) to the isosceles triangle as an approximation. This, in turn, is equivalent to approximating the arc by the chord, an approximation which improves as the angle decreases toward zero. Therefore, one concludes that

$$\lim_{\alpha \to 0} c_j = \beta_j \quad (20)$$

and can use Equations (18) and (19) with the present scheme to compute $F(\xi, \theta)$ for small angles α. Sparrow's Figure 2 (*1*) clearly shows the approach to equality of the fN_{Re} products computed for the two geometries as α gets small, his curves being nearly coincident for $\alpha \leq 10$ deg.

Figure 6 is a plot of the theoretical curve of $(N_{Re})_{c1}$ as a function of apex angle α computed according to the above described methods.

EXPERIMENTAL STUDY

Apparatus

In order to obtain data which were sufficiently precise and extensive* to permit determination of the two predicted critical Reynolds numbers, a series of aluminum ducts of various isosceles triangular cross sections were constructed and used in a recirculating flow loop illustrated schematically in Figure 7.

Flow Loop. The flow loop consisted of a 900-gal. storage tank from which the fluid was drawn by a large gear pump. From the pump the fluid could, by means of a bypass valving arrangement, be diverted back to the main storage tank or be pumped through a heat exchanger and into the test duct. Upon leaving the test duct, the fluid entered the flow rate measuring manifold. The latter consisted of two parallel lines, one leading back to the storage tank and the other leading to a weighing tank mounted on platform scales. These two exit lines contained

* A survey of the literature showed that no data of sufficient precision existed to permit determination of the two critical Reynolds numbers. Carlson's data (*3*) were too scanty to be used.

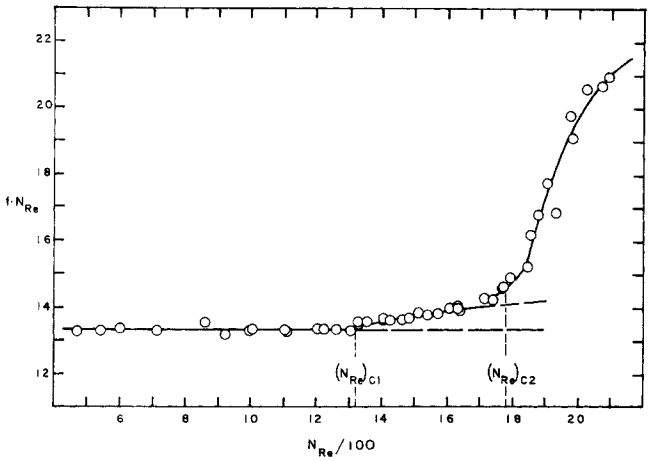

Fig. 13. Experimental friction loss data obtained in α = 22.5 deg. duct.

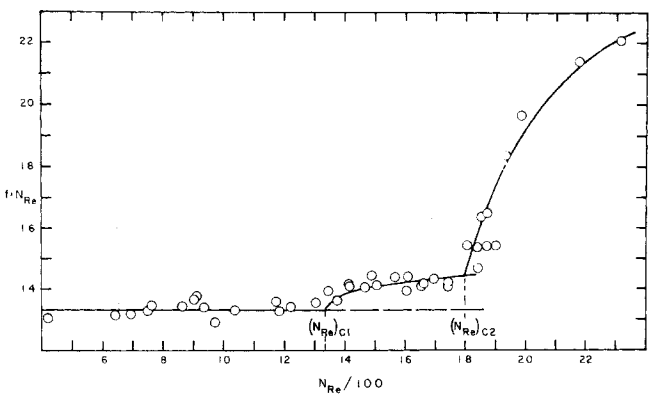

Fig. 14. Experimental friction loss data obtained in α = 30 deg. duct.

TABLE 1. ISOSCELES TRIANGULAR DUCT DIMENSIONS

Apex angle, deg.	Height, in.	Base, in.	D_H*, in.	D_H†, in.
5	5.000	0.437	0.418	0.409
15	3.000	0.790	0.693	0.674
30	2.000	1.071	0.822	0.804
45	1.750	1.450	0.969	0.967
60	1.500	1.732	1.000	1.028
75	1.375	2.110	1.041	1.024
90	1.250	2.500	1.036	1.034

Length of ducts: 12 ft.
* Measured.
† Corrected to fit Sparrow's theoretical results.

identical compressed air operated Delta* valves. The valve air supply was so arranged that when one valve was open the other was closed and vice versa. Thus, by simply throwing a switch, the flow stream could be diverted very quickly from the return line to the weigh tank line. The flow rates were measured by timing the interval required for the collection of a convenient weight of fluid. The reproducibility of these flow rate measurements was ± 0.5%.

Pressure losses were measured with a two-fluid U tube manometer. The manometric fluid used was Merriam red indicator (nominal sp. gr. 2.96). Because the system fluid (aqueous solutions of polyethylene glycol†) was found to be slightly

* Trade mark of the Galligher Company for compressed air operated, rubber lined, squeeze valves.

† Obtained from the Dow Chemical Company. This moderate molecular weight material is water soluble and in the concentration range used made a Newtonian solution with viscosity of about 60 to 70 centipoises.

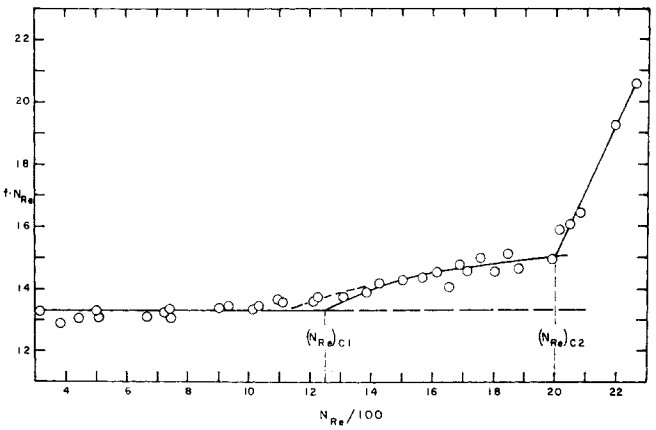

Fig. 15. Experimental friction loss data obtained in α = 37.5 deg. duct.

soluble in the Merriam red oil, careful measurements of the manometric fluid density were made with a calibrated pycnometer before every set of measurements to insure that the values used in the calculations corresponded to the fluid actually used in the manometer.

Because the viscosity of the polyethylene gylcol solutions is strongly temperature and concentration dependent, considerable care was exercised in maintaining the operating temperature constant prior to making an individual measurement. In addition to this precaution, the viscosity-temperature curve was determined experimentally for a sample of the system fluid collected either before or after a series of measurements. This was accomplished with the aid of a certified Ubbelohde viscometer in a carefully temperature controlled water bath. When all pertinent errors were considered, by using the error analysis of Mickley et al. (*9*) the composite error in the product $f \cdot N_{Re}$ was estimated at ±3.2%.

Duct Design. A very important factor in obtaining precise data in triangular ducts is the basic duct design. Previous investigators had difficulties with obtaining sharp corners (*11*) maintaining dimensional stability (*12*), and avoiding leakage at the corners (*3, 10*). In order to eliminate these difficulties and to provide maximum accessibility to the duct from all walls, the ducts were designed (*13*) to have a three-piece construction, illustrated in Figure 8. Each of the three side pieces of the duct was carefully machined from heavy rolled aluminum* stock. The three mating surfaces were ground flat, and each contained a longitudinal groove into which was placed a linear rubber O ring gasket to provide a positive liquid or gas tight seal. The three side plates were bolted together as illustrated on all three corners at 3-in. intervals axially down the duct. The resulting duct was very rigid, dimensionally consistent, and leak free. Pressure taps were carefully drilled and deburred in the base plate of the duct along the center line at various positions. Sharp edged entrances and exits were arranged by means of flanges which contained mating triangular shaped holes and were bolted directly to the ends of the ducts. These flanges in turn bolted to standard 10-in. pipe flanges attached to the piping of the flow loop. The details of the ducts used are tabulated in Table 1.

Experimental Results

In order to test the validity of the error analysis and the overall consistency of the various instruments and their calibrations, a series of measurements were made in a straight, smooth pipe. These data are compared in Figure 9 with theoretical curves (*14*). The measurements obtained in the various isosceles triangular ducts are presented as plots of $f-N_{Re}$ vs. N_{Re} in Figures 10 through 16. The values of $(N_{Re})_{c1}$ determined from these data are plotted in comparison with the theory in Figure 17, and the values of $(N_{Re})_{c2}$ determined from the present data and from literature data are presented as a function of α in Figure 18.

* Aluminum was used solely for considerations of weight of the finished duct.

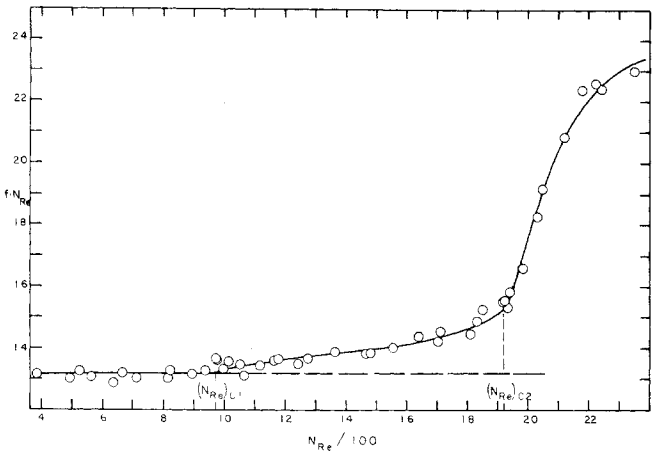

Fig. 16. Experimental friction loss data obtained in $\alpha = 45$ deg. duct.

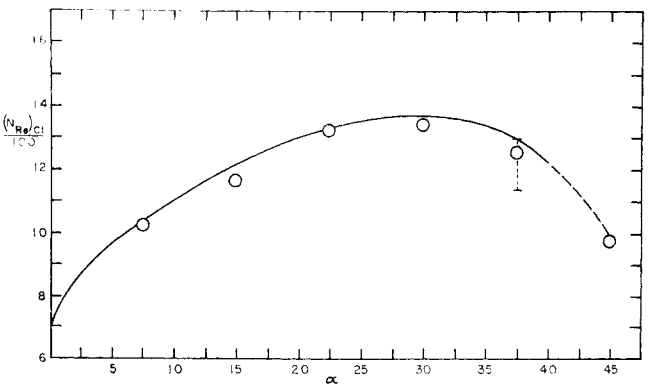

Fig. 17. Comparison of experimental values of $(N_{Re})_{c1}$ as calculated from experimental friction loss data with theoretical curve.

Discussion of Results

Because of the sharpness of the angles in the duct cross sections, precise measurement of the duct altitudes was very difficult, the errors of several successive measurements made by independent observers averaging as much as ±0.010 in. This error, although rather small, when accounted for in the calculation of the $f \cdot N_{Re}$ product resulted in shifting the mean values of the data in the laminar region by 2 to 3%. This shift in mean was approximately equal to the cumulative error band due to the remainder of the experimental variable uncertainties. Furthermore, the shift was not always in the same direction relative to the theoretical values. Figure 19 shows a plot of the laminar flow values of the mean $f \cdot N_{Re}$ product, based upon the best as-measured altitudes, in comparison with Sparrow's theoretical (*1*) values. The precision levels of the laminar data were felt to indicate that a more precise value of D_H could be obtained from flow measurements than from caliper measurements. Consequently, after the data of Figure 19 were obtained and evaluated, the mean of the laminar flow data for each duct was fitted to Sparrow's theoretical value of $f \cdot N_{Re}$, and the value of D_H appropriate to the duct was back calculated from this fit. These values of D_H are tabulated in Table 1 and were used in all subsequent calculations. A correction to an as-measured basis can easily be made by using the differences between these values and the measured values which are also tabulated in Table 1.

Examination of the data in Figure 10 clearly reveals that for this duct only one transition can be observed at $N_{Re} = 1{,}340$. Such behavior is characteristic of the parallel plate channel limiting form, but the magnitude is consistent with the $(N_{Re})_{c2}$ curve in Figure 18. Taking the height to base ratio as a crude comparison to the aspect ratio* of a rectangle, we see that for $\alpha = 2.5$ deg., $s/2b = 1/(2 \tan \alpha) = 11.45$. It was observed by Hanks and Ruo (*8*) that rectangular ducts having aspect ratios greater than 8 or 10 were within 1 to 2% of their limiting parallel plate behavior. From Figure 17 it appears that a similar criterion does not apply to isosceles triangles. Therefore, the different behavior of the data in Figure 10 cannot be explained in this manner. Apparently, for such a small angle duct, the first transition is masked by the experimental scatter of the data and could not be measured with the present apparatus.

The data for the $\alpha = 30$ deg. duct are most interesting in that they clearly reveal the existence of two distinct breaks in the curve. As intimated in the theoretical analysis, the details of the turbulent flow field generated by the symmetrical but nonuniform stress distribution apparently have a strong influence on the transitional flow. Thus, even though a relatively high degree of symmetry exists in the equilateral triangular duct, it does not behave in the transition region in a manner similar to a pipe. In order to verify this observation, a complete and independent second set of measurements was made (*15*) for this duct, and the results of Figure 14 were duplicated exactly.

Figures 15 and 16 show a feature of the data for $\alpha > 30$ deg. which differs characteristically from that for $\alpha < 30$ deg. In the vicinity of $(N_{Re})_{c1}$, the data deviate from the laminar value more gradually and without the sharply defined jump observed for the $\alpha < 30$ deg. ducts. This makes the determination of the exact value of $(N_{Re})_{c1}$ much more difficult. This difference is probably due to the fact that for $\alpha < 30$ deg., two walls are contributing to the instability of the flow, while for $\alpha > 30$ deg., only one wall contributes. The other characteristic of these data is that the second transition is likewise somewhat less sharply defined.

The data in Figures 10 to 16 were analyzed and the two critical values of N_{Re} determined. In Figure 17 the experimental values of $(N_{Re})_{c1}$ are compared with the theoretical curve. With the exception of the $\alpha = 37.5$ deg. duct, all of the data fall within the limits of experimental uncertainty of the theoretical curve. The data for the 37.5 deg. duct are seen from Figure 15 to be quite smeared out in this region. This fact is indicated in Figure 17 by the rather broad error band attached to this particular datum point. The existence of the theoretically predicted minimum and maximum lower critical Reynolds numbers as a function of α is clearly verified by the data for all except the $\alpha = 2.5$ deg. duct.

The results of Figure 17 indicate the effect of symmetry of the wall shear stress distribution on the stability of flow. The stability of the flow steadily increases as the asymmetry of the triangle decreases toward the symmetry of the equilateral triangle. At the symmetrical equilateral condition, the stability has increased to the maximum level. As α increases above 30 deg., the asymmetry effect again results in a decrease in stability. It is therefore clear that high degrees of asymmetry associated with a stress distribution serve to decrease the stability of the flow field and, hence, the extent of laminar flow possible in the duct. Because of this fact, it would appear that

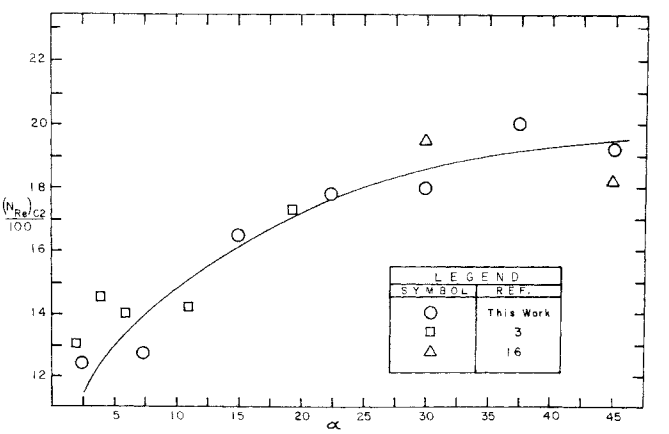

Fig. 18. Empirical curve showing proposed variation of $(N_{Re})_{c2}$ with α as determined from available data.

* Length of large side to small side.

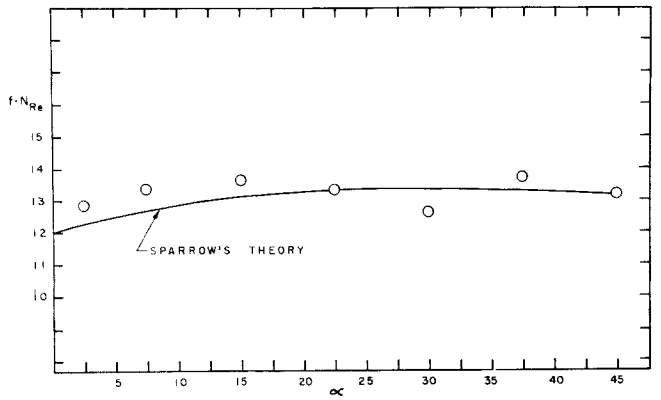

Fig. 19. Comparison of measured laminar values of the product $f\ N_{Re}$ based on caliper measured duct dimensions with theoretical curve calculated from Sparrow's equations as a function of apex half angled.

the use of a highly asymmetric pattern in compact heat exchangers should increase the heat transfer characteristics because it would make the flow more highly turbulent at a given Reynolds number. This is consistent also with the observations of Hanks and Brooks (*4*) that turbulent eddies penetrate into the apex region when the Reynolds number exceeds the upper critical value by a modest amount.

Since no theoretical calculation of the variation of $(N_{Re})_{c2}$ with α is possible, one must resort to an empirical determination of the curve. This has been done, and the results are presented in Figure 18. In addition to the present data, the literature data of Carlson (*3, 10*) and Nikuradse (*16*) were analyzed by the above technique, and the values of $(N_{Re})_{c2}$ obtained from their data are included in Figure 18. The reason that no corresponding data points are to be found in Figure 17 is that none of these authors had data which were sufficiently precise to even show a value of $(N_{Re})_{c1}$. Carlson's (*10*) data are rather scarce and not nearly so precise as those of the present study, and his values of $(N_{Re})_{c2}$ are subject to quite wide variation depending upon where one draws the curve to approximate his nonlaminar data.

The curve drawn in Figure 18 is consistent with the similar curve in Figure 17 which was predicted theoretically. It is believed that the qualitative effect of the stress asymmetry should be the same for $(N_{Re})_{c2}$ as for $(N_{Re})_{c1}$.

Nikuradse's (*16*) two values are, at most, tentative, since he presented only one or two data points which were laminar flow. Actually, these nonturbulent points (*15*) had values of $f \cdot N_{Re}$ greater than the theoretical laminar values, and for this reason his critical Reynolds numbers were interpreted as $(N_{Re})_{c2}$. Nikuradse's (*16*) data appear to agree with the present results, which are much more certainly known.

CONCLUSIONS

The agreement between the data and theory in Figure 17 and the visual data presented by Hanks and Brooks (*4*) leads one to the conclusion that there does exist a special transitional regime of flow in this highly asymmetrically stressed flow system in which different portions of the flow field are simultaneously in stable laminar and turbulent flow. The present work represents the first theoretical prediction of the existence of such a phenomenon.

A further conclusion of interest is that at a given Reynolds number in excess of $(N_{Re})_{c1}$, the more asymmetric ducts with $\alpha < 30$ deg. will be in a state of more turbulent motion than the symmetric 30 deg. duct. This is of possible significance in considering heat transfer behavior of compact heat exchangers which utilize the asymmetric triangular flow geometry.

ACKNOWLEDGMENT

This work was supported by the National Science Foundation under grants GK-550 and GK-1922. All numerical computations were performed with the Brigham Young University Computer Center's IBM-7040 digital computer. We wish to thank Fred Childs of the Brigham Young University Research Shop for constructing the triangular test ducts.

NOTATION

A = cross-sectional area of duct
b = base of triangle
c_j = Fourier coefficient
D_H = hydraulic diameter = 4 (cross-sectional area)/(wetted perimeter)
f = friction factor
$\mathbf{f}$ = body force vector
F = function defined by Equation (4)
G = function of angle α defined by Equation (6)
I_j = function defined by Equation (10)
K = stability parameter
N_{Re} = Reynolds number
p = pressure
r = radial variable of polar coordinate system
s = altitude of isosceles triangle
u = $v_z/\langle v_z \rangle$
$\mathbf{v}$ = velocity vector
v_z = axial component of $\mathbf{v}$
$\langle v_z \rangle$ = area mean value of v_z
x = Cartesian coordinate
y = Cartesian coordinate
z = axial distance

Greek Letters

α = apex half angle
β_j = function defined by Equation (19)
ζ = y/b
θ = polar coordinate angle
λ_j = eigenvalue defined by Equation (5)
μ = fluid viscosity
ρ = fluid density
ξ = r/s

LITERATURE CITED

1. Sparrow, E. M., *AIChE J.*, **8**, 599 (1962).
2. Eckert, E. R. G., and T. F. Irvine, Jr., *Trans. Am. Soc. Mech. Engrs.*, **78**, 709 (1956).
3. Carlson, L. W., and T. F. Irvine, Jr., *J. Heat Transfer*, **83**, 441 (1961).
4. Hanks, R. W., and J. C. Brooks, *AIChE J.*, **16**, 483 (May, 1970).
5. Hanks, R. W., *ibid.*, **9**, 45 (1963).
6. *Ibid.*, **15**, 25 (1969).
7. Kaplan, W., "Advanced Calculus," pp. 125-127, Addison-Wesley, Reading, Mass. (1956).
8. Hanks, R. W., and H. C. Ruo, *Ind. Eng. Chem. Fundamentals*, **5**, 558 (1966).
9. Mickley, H. S., T. K. Sherwood, and C. E. Reed, "Applied Mathematics in Chemical Engineering," 2 ed., Chapt. 2, McGraw-Hill, New York (1957).
10. Carlson, L. W., M.S. thesis, Univ. Minn., Minneapolis (Aug., 1959).
11. Eckert, E. R. G., and T. F. Irvine, Jr., "Proceedings Fifth Midwest Conference Fluid Mechanics," p. 122, Univ. Mich. Press, Ann Arbor (1957).
12. Cremers, C. J., and E. R. G. Eckert, *J. Appl. Mech.*, **29**, 609 (1962).
13. Gudmundsen, S. L., B.E.S. thesis, Brigham Young Univ., Provo, Utah (May, 1964).
14. Hanks, R. W., *AIChE J.*, **14**, 691 (1968).
15. Cope, R. C., M.S. thesis, Brigham Young Univ., Provo, Utah (May, 1968).
16. Nikuradse, J., *Ing. Arch.*, **1**, 306 (1930).

Manuscript received July 10, 1968; revision received October 30, 1968; paper accepted November 13, 1968. Paper presented at AIChE Los Angeles meeting.